MATERIALS SCIENCE

Enhancing strength and ductility via crystalline-amorphous nanoarchitectures in TiZr-based alloys

Kaisheng Ming[1,2,3]†, Zhengwang Zhu[4]†, Wenqing Zhu[5,6], Ben Fang[5,6], Bingqiang Wei[3], Peter K. Liaw[7], Xiaoding Wei[5,6]*, Jian Wang[3]*, Shijian Zheng[1,2]*

Crystalline-amorphous composite have the potential to achieve high strength and high ductility through manipulation of their microstructures. Here, we fabricate a TiZr-based alloy with micrometer-size equiaxed grains that are made up of three-dimensional bicontinuous crystalline-amorphous nanoarchitectures (3D-BCANs). In situ tension and compression tests reveal that the BCANs exhibit enhanced ductility and strain hardening capability compared to both amorphous and crystalline phases, which impart ultra-high yield strength (~1.80 GPa), ultimate tensile strength (~2.3 GPa), and large uniform ductility (~7.0%) into the TiZr-based alloy. Experiments combined with finite element simulations reveal the synergetic deformation mechanisms; i.e., the amorphous phase imposes extra strain hardening to crystalline domains while crystalline domains prevent the premature shear localization in the amorphous phases. These mechanisms endow our material with an effective strength–ductility–strain hardening combination.

INTRODUCTION

Strength and ductility are arguably two important mechanical properties of structural materials, while they are mutually exclusive in general, referred to as the strength-ductility trade-off (*1*–*3*). Crystalline materials can be strengthened through refining grains and/or introducing secondary phases, because the interfaces, such as grain boundaries (GBs) and phase boundaries, impede the motion of dislocations (*4*–*9*). However, the ductility is generally reduced owing to the sacrifice of the strain hardening capability (*10*–*12*). Metallic glasses display much higher strength than that of their crystalline counterparts but have a very low plastic strain (<2%) before catastrophic brittle fracture, due to the shear band softening effect (*13*–*15*). The metallic glass matrix composites (MGMCs), composed of microscale crystalline dendrites distributed in a continuous amorphous matrix, can reconcile strength and ductility. However, most conventional MGMCs have no strain hardening capabilities under tension, and thus, their strength cannot reach that of bulk metallic glasses counterparts as a result of soft crystalline phases or shear band softening effect in amorphous phases (*13*).

Unlike crystalline materials, metallic glasses display an increased deformability as the characteristic dimension is reduced to nanoscale (*16*–*22*). Recently, it is demonstrated that the shear banding can be effectively prevented in crystalline-amorphous nanolaminates and nanograins with metallic glass shells as the size of amorphous phases is smaller than 100 nm (*19*, *20*, *23*). Therefore, crystalline-amorphous composites comprising nano-sized amorphous and crystalline phases are expected to achieve high strength and high ductility simultaneously. Although crystalline-amorphous nanolaminates exhibit high strength and measurable plasticity, as the loading is normal to the interface plane, compressive instability, such as bulking, often happens, as the loading is parallel to the interface plane (*24*–*29*). The nanograins enwrapped by nano-sized metallic glass shells lack strain hardening and ductility under tension loading due to the strain localization along amorphous GBs (AGBs). It should be noted that crystalline and/or amorphous phases are separated in the above-mentioned composites, weakening the interaction between two phases, thus leading to the early onset of plastic instability. To enforce the interaction between two phases, nano-sized crystalline and amorphous phases should form three-dimensional (3D) interconnected structures, in which randomly oriented amorphous-crystalline interfaces (ACIs) discretize the formation of localized shear bands, and the amorphous phase impedes the propagation of dislocations and shear bands in the crystalline phase. Moreover, the 3D-interconnected crystalline and amorphous structure can eliminate the anisotropic plasticity associated with nanolaminates, ensuring the isotropic plasticity.

Here, we design and synthesize a unique TiZr-based nanoscale crystalline-amorphous composites (nano-CACs) by melt spinning with extremely high rates of cooling. The TiZr-based nano-CAC consists of micro-sized equiaxed grains with nano-width AGBs. Each micrograin comprises nano-sized metastable crystalline phases and amorphous phases that are arranged in the form of 3D-networked nano-bands, which are referred to as 3D bicontinuous crystalline-amorphous nanoarchitectures (3D-BCANs). The metastable crystalline phase plastically deforms through dislocation slip and martensitic phase transformation, while the nano-sized amorphous phases exhibit homogeneous flow behavior due to interface constraints. Compared with both individual constituent crystalline and amorphous phases, an exceptional strength–ductility–strain hardening combination is realized due to the co-deformation mechanism associated with the 3D-BCANs coupled with transformation-induced plasticity. Our materials with 3D-BCANs also exhibit much superior strength and ductility than that of conventional MGMCs. This study offers a strategy for producing strong

[1]State Key Laboratory of Reliability and Intelligence of Electrical Equipment, Hebei University of Technology, Tianjin 300130, China. [2]School of Materials Science and Engineering, Hebei University of Technology, Tianjin 300130, China. [3]Mechanical and Materials Engineering, University of Nebraska-Lincoln, Lincoln, NE 68588, USA. [4]Institute of Metal Research, Chinese Academy of Sciences, Shenyang 110016, China. [5]State Key Laboratory for Turbulence and Complex System, Department of Mechanics and Engineering Science, College of Engineering, Peking University, Beijing 100871, China. [6]Beijing Innovation Center for Engineering Science and Advanced Technology, Peking University, Beijing 100871, China. [7]Department of Materials Science and Engineering, The University of Tennessee, Knoxville, TN 37996, USA.
*Corresponding author. Email: xdwei@pku.edu.cn (X.W.); jianwang@unl.edu (J.W.); sjzheng@hebut.edu.cn (S.Z.)
†These authors contributed equally to this work.

and ductile crystalline-amorphous composite through 3D nano-architecting design.

RESULTS AND DISCUSSION

Bulk $Ti_{47.2}Zr_{35.9}Cu_{5.5}Be_{11.4}$ [atomic % (at %)] alloys consisting of TiZr-rich crystalline phases and CuZr-rich amorphous phases were produced by melt spinning, copper mold suction casting, and arc melting at the cooling rates decreasing from 10^6 to 10 K/s, and the characteristic sizes of both crystalline and amorphous phases decrease with the increase in cooling rate (Fig. 1, A to C, and fig. S1). For the ribbon sample prepared by melt spinning with a cooling rate of ~10^6 K/s, we obtained TiZr-based nano-CACs with the characteristic sizes of both crystalline and amorphous phases less than 50 nm. The transmission electron microscopy (TEM) bright-field (BF) micrograph in Fig. 1D with the corresponding selected-area electron diffraction (SAED) pattern inset, taken from the plane view of the ribbon sample (fig. S2A), clearly reveals equiaxed grains with an average grain size of 1.5 μm, which is identified to be the β phase with a body-centered cubic (bcc) structure. Orientation analysis by electron backscatter diffraction (EBSD) in fig. S2 (B and C) indicates the presence of a weak crystallographic texture. The higher magnification of BF-TEM image in Fig. 1E, with the corresponding SAED patterns in Fig. 1 (F and G), shows two grains with different

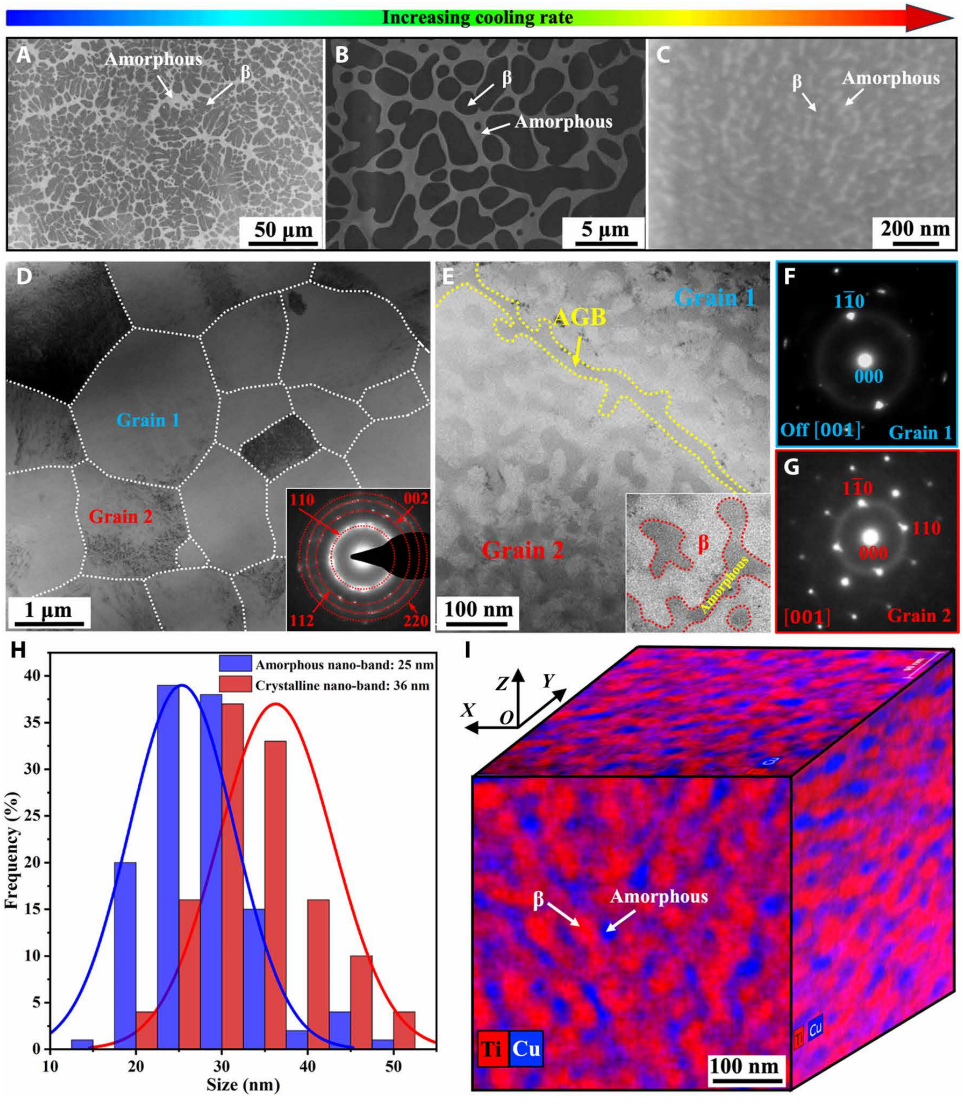

Fig. 1. TiZr-based nano-CACs consisting of 3D-BCAN micrograins. Scanning electron microscope (SEM) images of the samples prepared by (**A**) arc melting, (**B**) copper mold suction casting, and (**C**) melt spinning, with cooling rates increasing from 10 to 10^6 K/s. The characteristic dimension of both crystalline and amorphous phases decreases with increasing the cooling rate, producing the (A) MGMCs, (B) micro-CACs, and (C) nano-CACs (inside one grain). Both MGMC and micro-CAC samples do not contain AGBs, while the nano-CAC sample contains AGBs. Typical 3D-BCANs in nano-CAC sample. (**D**) A plane-view BF-TEM image with a corresponding SAED pattern inset, showing the polycrystalline bcc-β phase structure. (**E**) BF-TEM image of a GB area. (**F** and **G**) The corresponding SAED patterns of grains 1 and 2, showing that each grain is composed of bicontinuous networked bcc-β nano-bands (bright contrast) and amorphous nano-bands (dark contrast). (**H**) Width distribution of amorphous and crystalline nano-bands. (**I**) 3D microstructures of the BCANs inside a grain highlighted in terms of the Ti and Cu distribution maps from the plane view (*XOY*) and side view (*XOZ* or *YOZ*) of nano-CAC sample, showing a nanoscale bcc-β phase (red band) and amorphous phase (blue band) arranged in a 3D-networked bicontinuous nanoarchitecture.

orientations separated by a band-like GB with an average thickness of ~15 nm (marked by yellow dashed lines). The band-like GBs are identified to be continuous amorphous phases enriched with Cu (fig. S3), which separates grain from grain, acting as AGBs. Intriguingly, each microscale grain is composed of single-crystal bcc-β nano-bands (bright contrast) and amorphous nano-bands (dark contrast) with a volume fraction of approximately 70 and 30%, respectively, as shown in Fig. 1E. The amorphous structure of the GBs and nano-bands inside the grain is confirmed by the diffuse diffraction halo in the SAED patterns in Fig. 1 (F and G) and the characteristic maze-like pattern in high-resolution TEM (HRTEM) images in fig. S3 (B and C). Note that there is essentially no contrast difference within β phases, suggesting that they are largely dislocation free (Fig. 1E, inset). Figure 1H summarizes the average widths of the β nano-bands and amorphous nano-bands, which are approximately 36 and 25 nm, respectively. The characteristic sizes of the β nano-bands and amorphous nano-bands in the samples are much smaller than the sizes of crystalline and amorphous phases in traditional MGMCs with the same chemical composition prepared with relatively low cooling rates, which are a few to tens of micrometers, as demonstrated in Fig. 1 (A to C) and fig. S1.

A cross-sectional TEM image of the nano-CAC sample shows the same microstructure as the plane-view image (fig. S4, A to C), which demonstrates that the amorphous phase and bcc-β phase form 3D networks with the nano-bands inside grains, leading to the formation of 3D-BCANs. Such a 3D-BCAN is quite different from the dendritic structure of traditional MGMCs from a viewpoint of spatial arrangement of crystalline and amorphous phases (*13*). The chemical composition analysis shows that the amorphous phase is Cu-enriched, while the β phase is Ti-enriched. The Zr element is distributed uniformly in both β and amorphous phases (fig. S4, D to H). The 3D-BCANs within a grain were highlighted in terms of Ti and Cu distribution maps from the plane view and cross-sectional view, as presented in Fig. 1I. On the basis of the chemical composition analysis, we thus refer to the constituent crystalline β phase and amorphous phase in the TiZr-based nano-CACs as TiZr-rich and CuZr-rich phases, respectively.

To investigate the mechanical response of the 3D-BCANs, we performed in situ scanning electron microscope (SEM) micropillar compression testing. Figure 2A shows representative compressive stress-strain curves of the single-crystal 3D-BCAN pillars that were fabricated from the TiZr-based nano-CAC samples using the focused ion beam (FIB), together with the single-crystal TiZr-rich β phase pillars and CuZr-rich amorphous pillars fabricated from the TiZr-based micro-CAC samples for comparison. The single-crystal 3D-BCAN

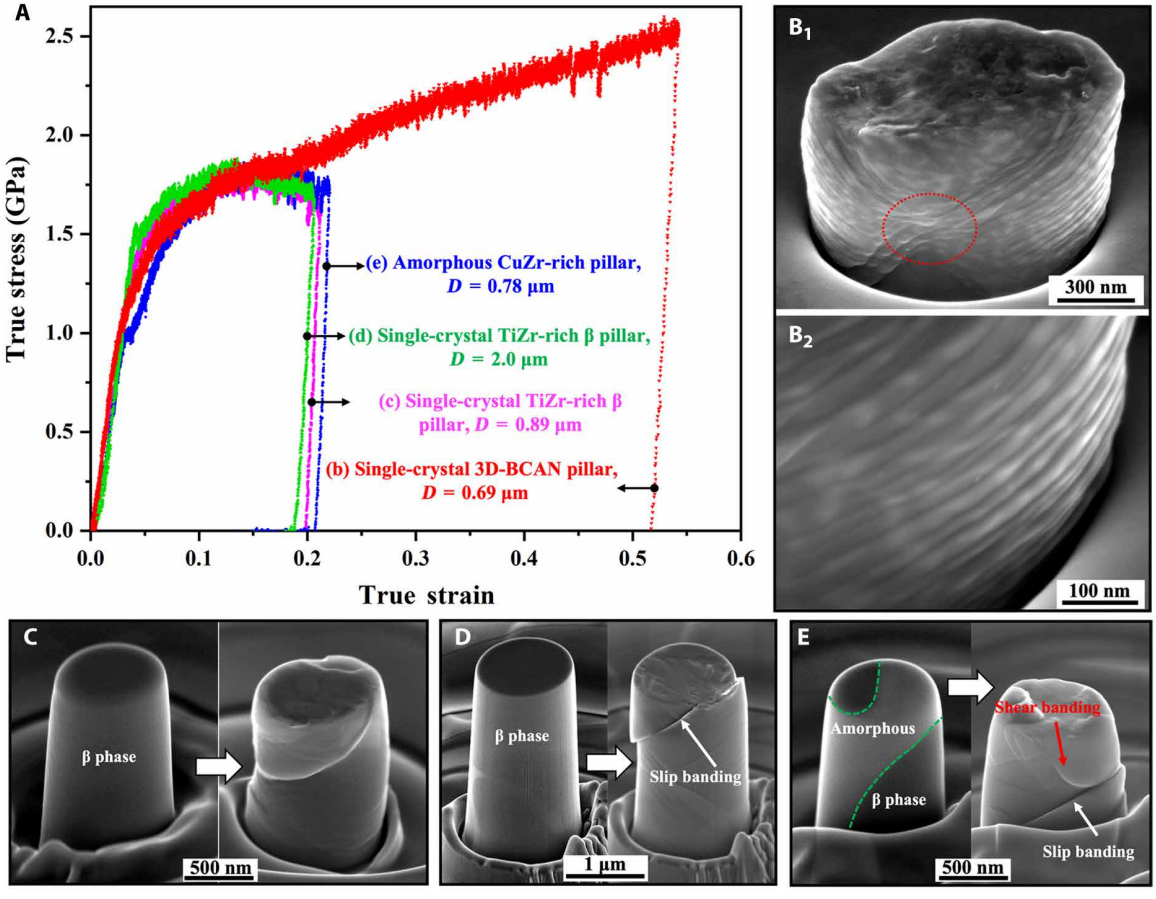

Fig. 2. Exceptional homogeneous deformability associated with strain hardening enabled by 3D-BCANs. (**A**) True stress-strain curves of the single-crystal 3D-BCAN pillars, compared with the single-crystal TiZr-rich β phase pillars and CuZr-rich amorphous pillars. (**B_1** and **B_2**) Single-crystal 3D-BCAN pillar after compression to 54% (with the loading direction close to $[011]_\beta$), showing homogeneous deformation through the formation of numerous nano-spaced shear bands. (**C** to **E**) Corresponding single-crystal TiZr-rich β phase pillars (with the loading direction close to $[011]_\beta$) and amorphous pillars before and after compression tests, showing the formation of the typical plastic instability by the localized slip banding (C and D) and shear banding (E).

pillar with a diameter of 0.69 μm displays a yield strength of 1.2 GPa and notable strain hardening, which results in a high flow strength exceeding 2.5 GPa and a high uniform compressive strain of >50% without onset of the plastic flow instability (Fig. 2A). The surface of the single-crystal 3D-BCAN pillar after deformation shows a high density of intersected nano-spaced shear bands (see Fig. 2, B_1 and B_2). Real-time imaging of the pillar deformation process demonstrates that the formation and propagation of multiple shear bands contribute to the large uniform plastic deformation. It must be pointed out that the mechanical response of single-crystal 3D-BCAN pillars shows slight orientation dependence, as demonstrated in fig. S5. In comparison, the single-crystal TiZr-rich β phase pillars and CuZr-rich amorphous pillars display comparable yield strengths but quick strain softening due to the onset of localized slip banding (Fig. 2, C and D) or shear banding (Fig. 2E). Nanoindentation results indicate that the elastic modulus and hardness of the 3D-BCANs falls in between those of the amorphous phase and β phase (fig. S6). The 3D-BCANs exhibit the superior homogeneous deformability associated with exceptional strain hardening. Therefore, the single-crystal 3D-BCAN pillars have much higher flow strengths and uniform strains. In addition, plastic deformation behavior of the single-crystal 3D-BCANs is also quite different from other single crystals, nanocrystalline metals, or amorphous micro/nano-pillars, where the intermittent discrete strain bursts appear in the stress-strain curves under uniaxial compression caused by the shear instability owing to the lack of strain hardening (*30*). Therefore, we speculated that the current unique structure of 3D-BCANs promotes the strain delocalization through enhancing the plastic deformation compatibility between the nanoscale β and amorphous phases (referred to as the 3D nano-sized synergistic effect). In what follows, we further validate our hypothesis through characterizing deformation mechanisms.

We performed TEM characterizations on the deformed 3D-BCAN pillars fabricated by FIB. The BF-TEM image of a single-crystal 3D-BCAN pillar after compression to 54% shows a flat barrel shape without any large shear plane/offset (Fig. 3A), further confirming the uniform plastic deformation. Such a large uniform strain is accommodated by the extensive nanoscale shear bands and dislocation accumulation. The enlarged TEM image in Fig. 3B corresponds to the shear band intersection region of the deformed pillar (marked by red circles in Figs. $2B_1$ and 3A), showing that the unstable propagation of shear bands can be blocked by shear band interactions (shear banding self-locking). The formation and propagation of extensive nanoscale shear bands contribute to the large plasticity, and the subsequent shear band self-locking prevents the onset of shear banding instability, resulting in a homogeneous plastic deformation. The obvious contrast difference between deformed and nondeformed regions in Fig. 3B demonstrates the significant dislocation accumulations in the deformed pillar, which contributes greatly to high

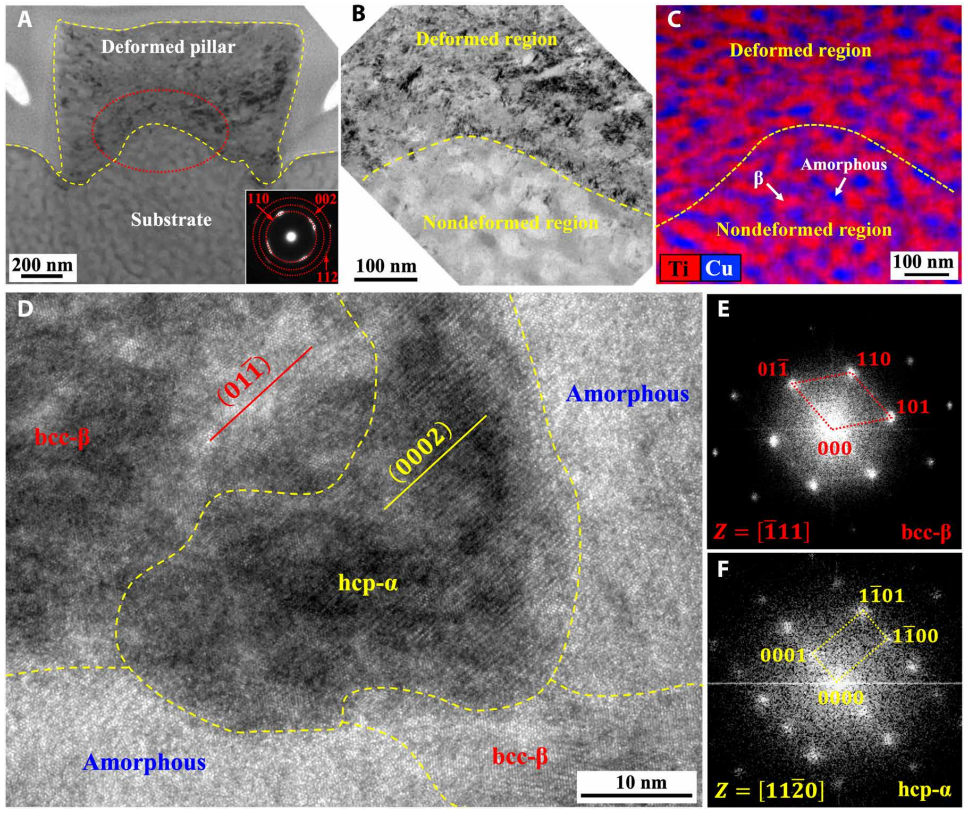

Fig. 3. Deformation mechanism of the single-crystal 3D-BCAN pillar. (**A**) Cross-sectional BF-TEM image of the deformed pillar (compressive strain of 54%) fabricated by FIB milling, with the corresponding SAED pattern inset. (**B**) An enlarged BF-TEM image of the intersection region of shear bands, showing the apparent boundary between deformed and nondeformed regions. (**C**) Corresponding TEM–energy dispersive spectroscopy mapping of Ti and Cu elements, presenting no apparent mixing between Ti and Cu elements after compression. (**D**) Corresponding HRTEM image of a deformed area around ACI showing the coexistence of three types of phases: bcc-β phase, hcp-α phase, and amorphous phase. (**E** and **F**) FFT images of the bcc-β phase and hcp-α phase, oriented in the [1$\bar{1}$1] and [11$\bar{2}$0] zone axes, respectively.

strain hardening. Shear bands are not observed in amorphous phases, indicating the uniform deformation in amorphous nano-bands. The corresponding Ti and Cu elemental mapping of the intersection region of shear bands shows that the nano-architecture of the crystalline phase and amorphous phase remains unchanged, and there is no apparent mixing between Ti and Cu elements after compression (Fig. 3C). This trend indicates that the nanoscale crystalline phase and amorphous phase exhibit exceptional plastic deformation compatibility. In contrast to the explosive martensitic phase transformation from the bcc-β phase to α phase with the hexagonal close-packed (hcp) phase in MGMCs (fig. S7), the deformation mechanism of the nano-sized bcc-β phase in nano-CAC is primarily dominated by dislocation motions. As illustrated by the SAED pattern of the deformed pillar inserted in Fig. 3A, the main phase in the deformed area is still the bcc-β phase, indicating that the 3D-BCANs make the martensitic phase transformation difficult. However, phase transformation (bcc-β → hcp-α) could occur scatteredly along ACIs owing to the large stress concentration, as shown in the HRTEM image in Fig. 3D. The corresponding fast Fourier transform (FFT) patterns of the bcc-β phase (Fig. 3E) and hcp-α phase (Fig. 3F) demonstrate the classic Burgers orientation relationship: $[\bar{1}11]_\beta \| [11\bar{2}0]_\alpha$ and $(01\bar{1})_\beta \| (0001)_\alpha$. The HRTEM image in Fig. 3D also shows that some regions (with dark contrast) in both bcc-β and hcp-α phases become blurred, indicating the deformation-induced severe lattice distortion due to dislocation accumulation. Such scattered phase transformation can relieve the stress concentration at ACIs and thus suppress the plastic flow instability and enable the high strain hardening associated with dislocation accumulations.

To understand the micro-mechanisms of the enhanced uniform strain and strain hardening capacity of 3D-BCANs, we simulated the compression response of the nano-CAC model via the finite element method using the crystal plasticity theory for crystalline phase and visco-plasticity theory for metallic glasses (*31*–*33*). The stress-strain curve (Fig. 4A) reproduces the high strength and strain hardening behavior of 3D-BCANs. The micro-mechanisms are unraveled. As shown in Fig. 4B, the dislocation-mediated plasticity is activated first in the crystalline domain at a compressive strain of 5%. This is in good agreement with the TEM characterizations on the 5%-strained 3D-BCAN pillar, as presented in Fig. 4C, where the crystalline domains contain numerous dislocations, demonstrating the occurrence of severe plastic deformation by the motion of dislocations. Then, as strain increases from 10 to 20%, embryos of shear bands start to nucleate in the amorphous regions but are interrupted by the crystalline domains, thus suppressing or delaying formation of mature shear bands (Fig. 4B). Meanwhile, the plastic deformation accumulates in crystalline domains, and the nano-CAC model continuously hardens up to a strain of 20% until multiple yet isolated slip bands emerge (evidenced by the severely concentrated plastic strain in Fig. 4B) at larger compressive strains. These randomly distributed severe strain concentrations around the ACIs can be effectively alleviated by the aforementioned scattered phase transformation observed by TEM as shown in Fig 3D.

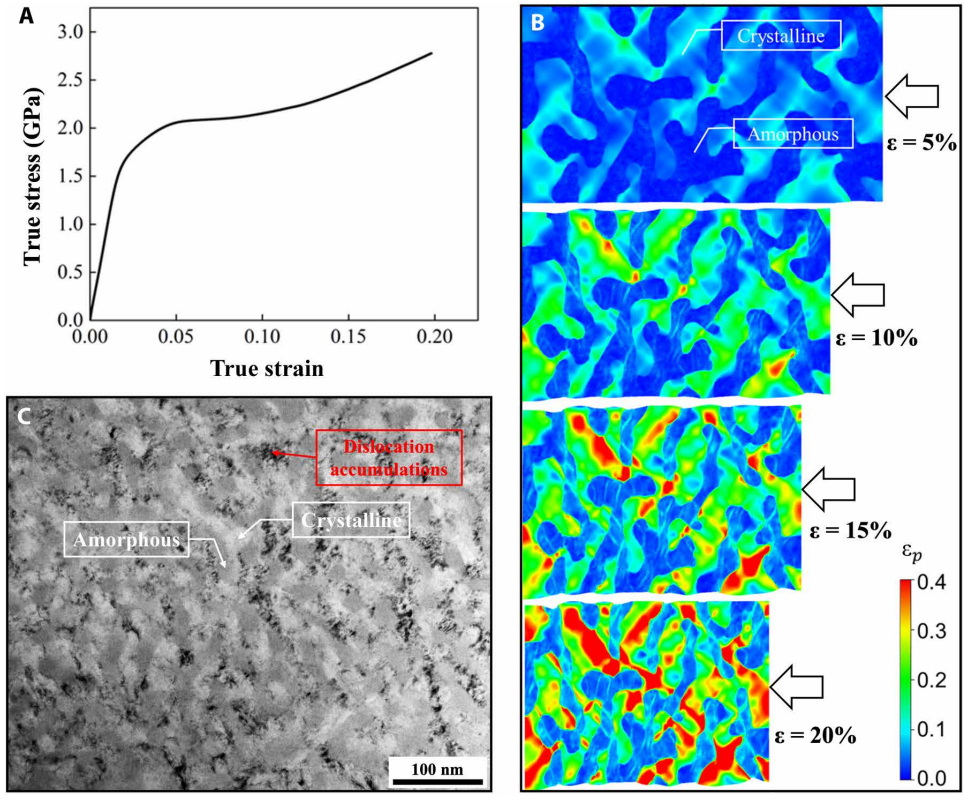

Fig. 4. Continuum modeling results for nano-CAC under compression. (**A**) Simulated stress-strain curve for the nano-CAC model. (**B**) Snapshots highlight the evolution of the equivalent plastic strain during compression at the strains of 5, 10, 15, and 20%. As the strain increases, plastic deformation first occurs in crystalline domains, followed by formation of embryos of shear bands in amorphous regions. (**C**) TEM image demonstrates the severe plastic deformation in the crystalline domains (highlighted by the excessive dislocation accumulations) at 5% compressive strain.

In addition to the enhanced plasticity and strain hardening capacity of 3D-BCANs under compression, the TiZr-based nano-CACs consisting of 3D-BCANs and AGBs exhibit an exceptional strength–ductility–strain hardening combination under tension, as compared with other micro-CACs in Fig. 5. Figure 5A shows representative tensile stress-strain curves of flat dog bone–shaped samples with a width of 2.0 to 4.5 μm and a thickness of 2.0 to 3.5 μm. The nano-CACs display a high yield strength of 1.80 ± 0.1 GPa, an ultimate tensile strength of 2.30 ± 0.1 GPa, and a good uniform tensile strain of 7.0 ± 1.0%, superior to micro-sized dendrite-reinforced TiZr- and CuZr-based micro-CACs (*34*–*43*), as illustrated in Fig. 5B. The nano-CACs exhibit an apparent strain hardening after yielding. At the homogeneous deformation stage, the stress-stain curve is relatively smooth, while after the uniform straining (>7.0%), several strain bursts and stress drops periodically appear on the stress-strain curve (Fig. 5A). Figure 5C shows a typical dog bone–shaped tensile sample before the in situ SEM tensile tests. After tension deformation, as presented in Fig. 5 (D to F), multiple shear bands are observed on the surface of the sample. The uniform plastic deformation corresponds to the formation and propagation of multiple shear bands and their interactions (Fig. 5, D and E), while the plastic instability (necking or shear banding) is attributed to the unstable propagation of shear bands (Fig. 5F), which leads to the strain bursts and stress drops on stress-strain curves. Similar to the micro-mechanisms in the compression test, the plastic deformations in crystalline and amorphous phases are compatible in nano-CACs under tension, thus effectively delaying the global shear localization. Correspondingly, the nano-CAC materials exhibit much improved ductility than the micro-CAC materials. Last, the slip bands in the crystalline phase and shear bands in the amorphous phase connect and form a main shear band, agreeing well with the experimental observations.

Compared with conventional micro-CACs with the debilitated deformation compatibility between microscale amorphous matrix and noncontinuous dendrites, the 3D-BCAN nano-architecting structure, accompanied by significant dislocation accumulations and discrete phase transformation in crystalline phases and homogeneous deformation in amorphous phases, can take full advantage of strong nanoscale amorphous phases and ductile crystalline phases, thus promoting 3D nano-sized synergistic effects. The strong 3D nano-architectured continuous amorphous nano-bands contribute to high strength. ACIs act as sources and barriers for dislocations, accommodating plastic deformation in crystalline phases and leading strain hardening due to significant dislocation accumulation inside continuous crystalline nano-bands. The local phase transformation (bcc-β → hcp-α) and dislocation annihilation at ACIs could effectively relieve stress-strain concentrations, avoiding cracking. A high

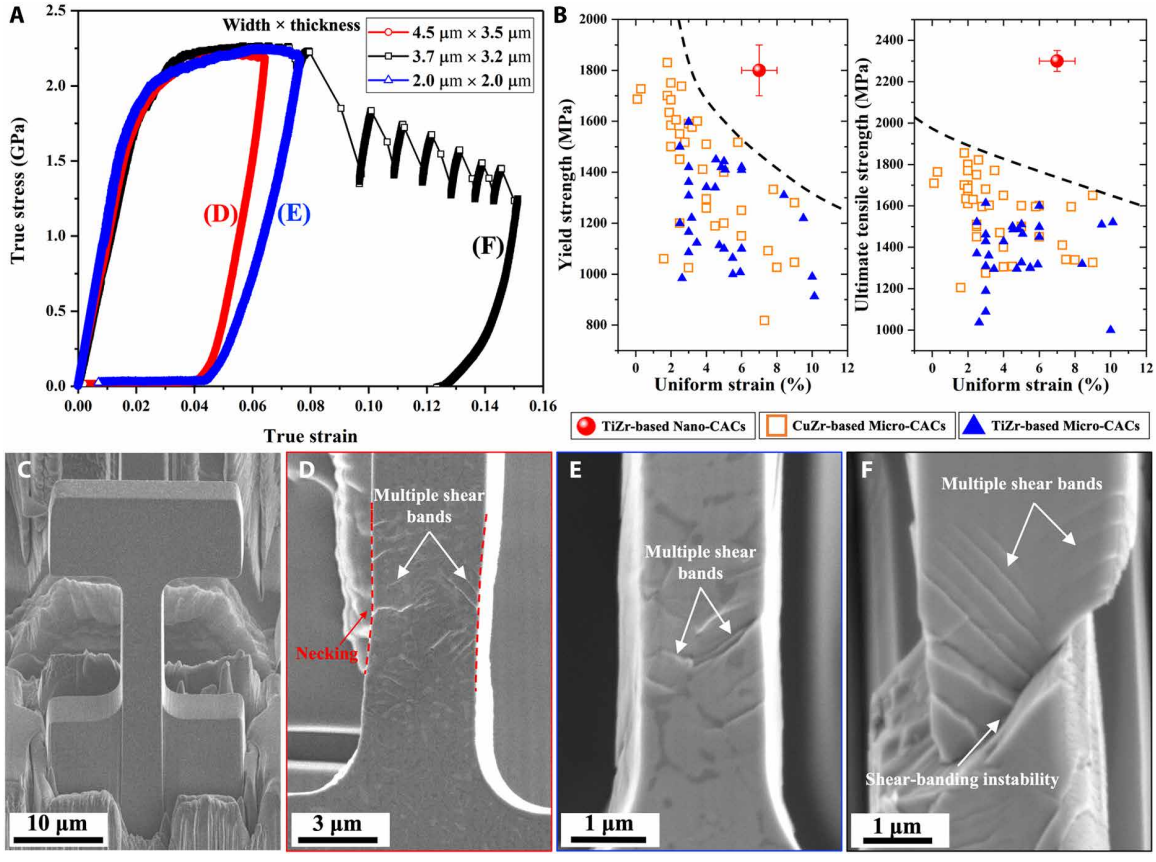

Fig. 5. Tensile behaviors of the TiZr-based nano-CACs consisting of 3D-BCAN micrograins. (**A**) Tensile stress-strain curves of the rectangular samples; (**B**) tensile properties of our TiZr-based nano-CACs, compared with conventional high-strength micro-CACs, showing an exceptional combination of strength and ductility in the current nano-CACs. (**C**) Typical dog bone–shaped tensile nano-CAC sample fabricated by FIB. (**D** to **F**) SEM images of the deformed nano-CAC samples with width × thickness values of 4.5 μm × 3.5 μm, 2.0 μm × 2.0 μm, and 3.7 μm × 3.2 μm, respectively. The nano-CAC samples exhibit homogeneous deformation through the propagation of multiple shear bands, accompanied by excellent strain hardening up to the true strain of ~7%.

density of ACIs associated with the 3D-BCAN nano-architecture helps facilitate multiple shear bands and phase transformation scatteredly. As a result, the homogeneous flow behavior of the nanoscale amorphous phase, scattered phase transformation, and pronounced dislocation activities inside a 3D nano-architectured crystalline phase result in homogeneous, isotropic plastic deformation of the current TiZr-based nano-CACs.

Last, to apply the strategy of 3D-BCANs in designing large-scale bulk materials, it is necessary to investigate the AGB effects on the mechanical behaviors of polycrystalline nano-CACs. The AGBs can restrain the plastic deformation among micro-sized nano-architectured grains and impede the unstable propagation of shear bands, which further increase the strength and strain hardening of nano-CACs but reduce the deformation compatibility across AGBs and thus decrease the ductility. Compared with single-crystal 3D-BCAN pillars (Fig. 2A), polycrystalline TiZr-based nano-CAC pillars composed of 3D-BCANs and AGBs exhibit a higher yield strength but a smaller uniform strain, as demonstrated in Fig. 6. For example, the compressive yield strength increases from 1.2 to ~1.8 GPa, but the uniform compressive strain decreases from 20 to ~8.5% when the pillar diameter increases from 0.65 to 5.5 μm (Figs. 2A and 6A). As exhibited in Fig. 6 (B_1, B_2, and C_1 to C_3), we could see a large number of nano-spaced, intersected shear bands on the surface of the deformed polycrystalline pillars. AGBs act as barriers to the transmission of shear bands from one grain to the adjacent grain (Fig. 6, B_1 and C_3), postponing or preventing the plastic instability associated with the unstable shear banding. The formation of multiple shear bands and their interactions contribute to the uniform compressive strains and apparent strain hardening. After a compressive strain of 20% for the 2.5-μm-diameter polycrystalline pillar (Fig. 6B_1) and 8.5% for the 5.5-μm-diameter polycrystalline pillar (Fig. 6C_1), plastic instability occurs, associated with shear banding across AGBs, i.e., the stress-strain curve is populated with intermittent discrete strain bursts (Fig. 6A). Further enhancement of the strength–ductility–strain hardening combination in nano-CACs can be achieved through tailoring the size of 3D nano-architectured grains, which has been generally accepted as grain-size effects in polycrystalline materials. In addition, we believe that the strategy of overcoming the strength-ductility trade-off with a 3D nano-architecture design could be applied extensively in composites containing different phases and/or structures.

In summary, the TiZr-based nano-CACs with a high yield strength of ~1.80 GPa, an ultimate tensile strength of ~2.30 GPa, and a uniform ductility of ~7.0% can be obtained by combining the metastable bcc-β phase and amorphous phase arranged in the 3D-networked bicontinuous nano-architectures. Such exceptional strength–ductility–strain hardening combination in nano-CACs originates from the 3D nano-architectures coupled with the transformation-induced plasticity. The metastable β phase plastically deforms through dislocation slip and phase transformation, while the nano-sized amorphous phase exhibits the homogeneous flow behavior due to interface constraints. The high density of ACIs associated with the 3D nano-architectures acts as a source and barrier for dislocations and phase transformation in crystalline phases and promotes the scattered activation of multiple shear bands, resulting in homogeneous plastic deformation and high strain hardening of nano-CACs. The present

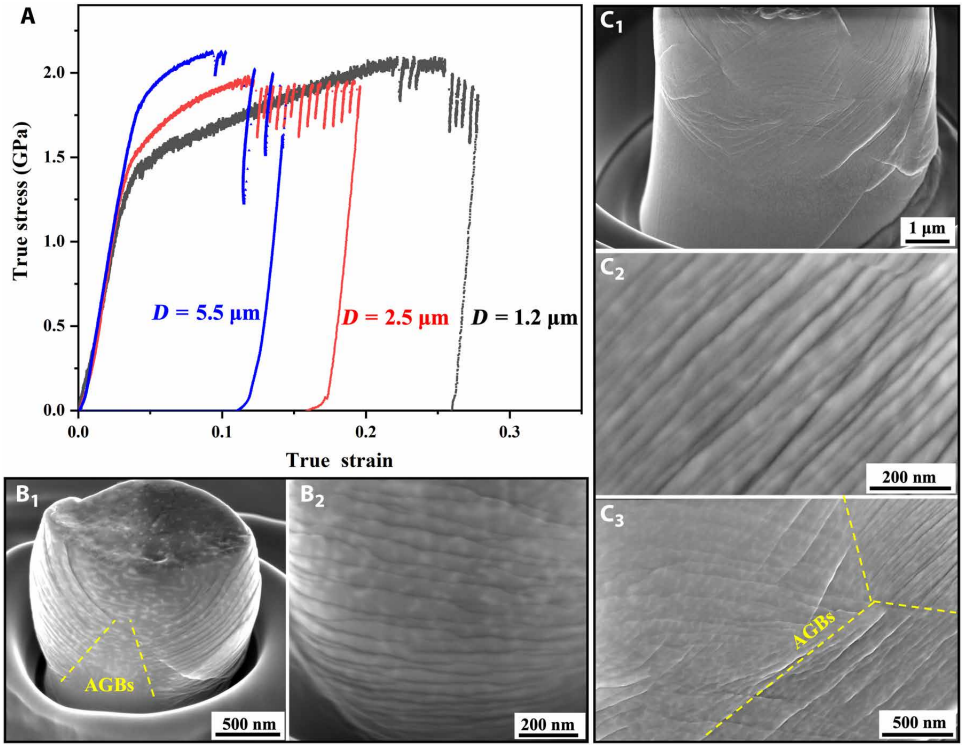

Fig. 6. Compressive behaviors of the polycrystalline TiZr-based nano-CACs consisting of 3D-BCAN micrograins and AGBs. (**A**) Compressive stress-strain curves for polycrystalline pillars with different diameters, showing the significant contribution of AGBs to mechanical properties. "*D*" indicates the diameter of the pillar. SEM images of the surface of the (**B_1** and **B_2**) 1.2-μm-diameter polycrystalline pillar and (**C_1** to **C_3**) 5.5-μm-diameter polycrystalline pillar after compression tests, showing multiple nano-spaced shear bands and their interactions with AGBs.

work demonstrated the enhancement of strength, ductility, and strain hardening capabilities of composites through a nano-structured architecture.

MATERIALS AND METHODS

Sample preparation

The ingots with a nominal composition of $Ti_{47.2}Zr_{35.9}Cu_{5.5}Be_{11.4}$ (at %) were first fabricated by conventional arc melting with high-purity elements (>99.95 at %) under a Ti-gettered argon atmosphere. The ingots were remelted at least five times to ensure chemical homogeneity. Then, the ingots were put inside the quartz tube with a 1-mm-diameter nozzle and were remelted in the induction coil and injected onto the surface of rotating copper roller to form a ribbon under a pressure of 0.01 to 0.05 MPa of high-purity argon. Last, the nano-CAC ribbon samples with a thickness of about 50 μm and a width of ~3 mm were prepared. The circumferential velocity was about 17 m/s for all the samples. The cooling rate was estimated to be 10^6 K/s. The quenching temperature was set to ~1723 K monitored by the infrared thermoscope. The temperature fluctuation was estimated to be ±10 K. More details about the single roller melt spinning method can be seen in our previous work (*44*). In addition, the bulk micro-CACs with the same chemical composition were prepared by copper mold suction casting with a relatively low cooling rate. The copper mold suction casting is a traditional material preparation method to fabricate MG and MGMCs. The detailed preparation process can be seen in our previous work (*45*). The macroscopic view of the samples with the same chemical composition prepared by melt spinning, copper mold suction casting, and arc melting can be seen in fig. S8 (A to C).

TEM characterizations and in situ SEM micro-pillar compression/tension testing

The microstructures of the samples were analyzed, using TEM (A FEI Tecnai G2 F20) coupled with energy dispersive spectroscopy and EBSD. Mechanical behavior of samples was measured, using in situ micro-tension/compression tests in a SEM at room temperature. The micropillars with diameters of 0.6 to 5.5 μm were fabricated from nano-CAC and micro-CAC samples with an FIB. The height-to-diameter ratio of each pillar was around 2 to 3. Flat dog bone–shaped tensile specimens with a width of 2.0 to 4.5 μm and a thickness of 2.0 to 3.6 μm were machined from the nano-CAC sample by FIB. To reduce the potential damage and contamination of the sample during FIB milling, the standard conditions for milling were used, such as 30 kV for the ion beam and decreasing currents for the different milling steps, 200, 100, and 50 pA, followed by finishing steps with 10 pA as the diameter of the pillars becomes smaller; 0.6-μm-diameter pillars were milled at 5 kV with similar currents for the milling and finishing. For all samples, the taper is no more than 5°. In situ SEM micromechanical testing was performed, using a PI85 PicoIndenter (from Hysitron) with a flat punch diamond tip under a displacement control mode at a loading rate of 5×10^{-3} s^{-1}. The representative in situ deformation movies can be seen in the Supplementary Materials (movies S1 and S2). Nanoindentation was conducted to evaluate Young's modulus, using a Hysitron TI950 nanoindenter with a diamond Berkovich tip. The Young's modulus of the current samples is summarized in fig. S6, which is used to correct the stress-strain curves. The different samples and corresponding mechanical properties are listed in table S1. Deformation mechanisms were further characterized on deformed pillars, using TEM. Specimens for TEM observations were prepared by using the FIB lift-out technique or grinding and polishing, followed by low-energy (3.5 keV) ion milling.

Continuum mechanics theory and finite element modeling

The 2D nano-CAC model (200 nm × 400 nm; fig. S8) containing the bicontinuous crystalline/amorphous nano-architectures was constructed by digitalizing a representative TEM photograph. The longitudinal direction was set to be [011] of the crystalline phase, which was also the loading direction for compression and tensile tests. Both models were meshed with 2 nm × 2 nm 2D quadrilateral elements (CPS4). A constant strain rate of 1×10^{-3}/s was used in all simulations.

The mechanical behavior of the crystalline phase is modeled by adopting the elastic-plastic constitutive formulations for single crystals that have been implemented by Huang through a user-defined material subroutine for ABAQUS (*32*). Here, we give a brief summary of the constitutive formulations. Under small deformation assumption, the total strain rate $\dot{\boldsymbol{\varepsilon}}$ is decomposed into the elastic and plastic parts

$$\dot{\boldsymbol{\varepsilon}} = \dot{\boldsymbol{\varepsilon}}^e + \dot{\boldsymbol{\varepsilon}}^p \tag{1}$$

in which the elastic strain rate $\dot{\boldsymbol{\varepsilon}}^e$ is related to the stress rate through the anisotropic linear elastic constitutive law

$$\dot{\boldsymbol{\sigma}} = \mathbf{C}:\dot{\boldsymbol{\varepsilon}}^e \tag{2}$$

On the basis of our nanoindentation results and referring to a previous study, the elastic constants (C_{11} = 159.2 GPa, C_{12} = 121.4 GPa, and C_{44} = 65.4 GPa) were used for β phase crystals.

The plastic strain rate $\dot{\boldsymbol{\varepsilon}}^p$ reads (*46*)

$$\dot{\boldsymbol{\varepsilon}}^p = \sum_{\alpha}^{N} \dot{\gamma}^{\alpha} \frac{(\mathbf{s}^{\alpha} \otimes \mathbf{m}^{\alpha} + \mathbf{m}^{\alpha} \otimes \mathbf{s}^{\alpha})}{2} \tag{3}$$

The vectors $\mathbf{m}^{\alpha}$ and $\mathbf{n}^{\alpha}$ are the unit vectors for the slip direction and normal to the slip plane of the slip system α, $\dot{\gamma}^{\alpha}$ is the shear rate for that system, and N is the number of the active slip system (here, N = 24 includes 12 ⟨111⟩{110} systems and 12 ⟨111⟩{112} systems; note that the ⟨111⟩{123} family were not considered as they are active mainly at high temperatures for BCC crystals). The following phenomenological kinetic law is used (*47*)

$$\dot{\gamma}^{\alpha} = \dot{\gamma}_0 \left| \frac{\tau^{\alpha}}{\tau_c^{\alpha}} \right|^{\frac{1}{m}} \mathrm{sign}(\tau^{\alpha}) \tag{4}$$

where τ^{α} is the resolved shear stress for slip system α, τ_c^{α} = 0.6 GPa is the slip resistance estimated from the uniaxial compression tests on the crystals, $\dot{\gamma}_0$ is the reference strain rate, and m is the rate sensitivity. In this study, we took $\dot{\gamma}_0 = 1 \times 10^{-3}$/s and m= 10 (*32*). The strain hardening due to dislocation replication and interactions is characterized by

$$\tau_c^{\alpha} = \sum_{\beta=1}^{N} h_{\alpha\beta} |\dot{\gamma}^{\beta}| \tag{5}$$

where $h_{\alpha\beta}$ are the slip hardening moduli. Here, we used very small hardening moduli ($h_{\alpha\beta} = 1 \times 10^{-6}$ GPa) to simulate an ideal elastic plastic behavior of the crystals.

The visco plasticity of the amorphous phase is modeled by the recently developed chemo-mechanical constitutive formulations for metallic glasses (*31*). For the detailed mathematical formulas, finite element implementation, and verification, the readers can refer to (*31*). The total strain rate of the amorphous phase is also decomposed into the elastic part and the plastic part

$$\dot{\boldsymbol{\varepsilon}} = \dot{\boldsymbol{\varepsilon}}^e + \dot{\boldsymbol{\varepsilon}}^p \quad (6)$$

in which $\dot{\boldsymbol{\varepsilon}}^e$ for the amorphous phase is related to the stress rate through an isotropic linear elastic constitutive law that consists of two elastic constants—Young's modulus $E = 127.1$ GPa and Poisson's ratio $\nu = 0.3$ estimated from our nanoindentation results. The plasticity of the amorphous phase was attributed to the evolution of the microstructural heterogeneity, which was characterized by the free volume ratio $\rho = 1 - \Omega^* c$ ($\Omega^* \sim 1 \times 10^{-29}$ m^3 is the atomic volume and c is the atomic concentration). At the beginning, a random ρ with an average of 0.01 was assigned to the nodes of the amorphous domains. The evolution of the free volume ratio distribution is fulfilled through the atomic flux driven by the chemical potential gradient, i.e., $\mathbf{j} = -Dc/k_BT\nabla\mu$ [$D \sim 3 \times 10^{-20}$ m^2/s is the diffusion coefficient (*48*), μ is the chemical potential, k_B is the Boltzmann constant, and T is the absolute temperature]. For the mathematical form of the chemical potential μ, the readers are referred to (*31*). Then, the plastic strain rate for the amorphous phase reads

$$\dot{\boldsymbol{\varepsilon}}_{\mathbf{p}} = \Omega^* \sqrt{(\nabla \mathbf{j})' : (\nabla \mathbf{j})'}\, N_p + \dot{J}_c \mathbf{I}/3 \quad (7)$$

in which $N_p = \boldsymbol{\sigma}'/\sqrt{\boldsymbol{\sigma}' : \boldsymbol{\sigma}'}$ is the flow direction, $\boldsymbol{\sigma}'$ is the deviatoric part of the stress tensor, and $\dot{J}_c = -\Omega^* \nabla \cdot \mathbf{j}$ is the dilatation rate. The chemo-mechanical model has been implemented in ABAQUS through a user-defined element subroutine.

SUPPLEMENTARY MATERIALS

Supplementary material for this article is available at https://science.org/doi/10.1126/sciadv.abm2884

REFERENCES AND NOTES

1. R. O. Ritchie, The conflicts between strength and toughness. *Nat. Mater.* **10**, 817–822 (2011).
2. M. E. Launey, R. O. Ritchie, On the fracture toughness of advanced materials. *Adv. Mater.* **21**, 2103–2110 (2009).
3. D. Raabe, C. C. Tasan, E. A. Olivetti, Strategies for improving the sustainability of structural metals. *Nature* **575**, 64–74 (2019).
4. M. A. Meyers, A. Mishra, D. J. Benson, Mechanical properties of nanocrystalline materials. *Prog. Mater Sci.* **51**, 427–556 (2006).
5. A. Ardell, Precipitation hardening. *Metall. Trans. A.* **16**, 2131–2165 (1985).
6. S. Jiang, H. Wang, Y. Wu, X. Liu, H. Chen, M. Yao, B. Gault, D. Ponge, D. Raabe, A. Hirata, M. Chen, Y. Wang, Z. Lu, Ultrastrong steel via minimal lattice misfit and high-density nanoprecipitation. *Nature* **544**, 460–464 (2017).
7. Z. Fu, L. Jiang, J. L. Wardini, B. E. MacDonald, H. Wen, W. Xiong, D. Zhang, Y. Zhou, T. J. Rupert, W. Chen, A high-entropy alloy with hierarchical nanoprecipitates and ultrahigh strength. *Sci. Adv.* **4**, eaat8712 (2018).
8. Z. Wang, W. Lu, H. Zhao, C. H. Liebscher, J. He, D. Ponge, D. Raabe, Z. Li, Ultrastrong lightweight compositionally complex steels via dual-nanoprecipitation. *Sci. Adv.* **6**, eaba9543 (2020).
9. B. Gao, Q. Lai, Y. Cao, R. Hu, L. Xiao, Z. Pan, N. Liang, Y. Li, G. Sha, M. Liu, Ultrastrong low-carbon nanosteel produced by heterostructure and interstitial mediated warm rolling. *Sci. Adv.* **6**, eaba8169 (2020).
10. K. Kumar, H. Van Swygenhoven, S. Suresh, Mechanical behavior of nanocrystalline metals and alloys. *Acta Mater.* **51**, 5743–5774 (2003).
11. J. Schiøtz, F. D. Di Tolla, K. W. Jacobsen, Softening of nanocrystalline metals at very small grain sizes. *Nature* **391**, 561–563 (1998).
12. X. Ke, J. Ye, Z. Pan, J. Geng, M. F. Besser, D. Qu, A. Caro, J. Marian, R. T. Ott, Y. M. Wang, Ideal maximum strengths and defect-induced softening in nanocrystalline-nanotwinned metals. *Nat. Mater.* **18**, 1207–1214 (2019).
13. J. Qiao, H. Jia, P. K. Liaw, Metallic glass matrix composites. *Mater. Sci. Eng. R Rep.* **100**, 1–69 (2016).
14. W. H. Wang, C. Dong, C. Shek, Bulk metallic glasses. *Mater. Sci. Eng. R Rep.* **44**, 45–89 (2004).
15. M. Telford, The case for bulk metallic glass. *Mater. Today* **7**, 36–43 (2004).
16. J. Luo, J. Wang, E. Bitzek, J. Y. Huang, H. Zheng, L. Tong, Q. Yang, J. Li, S. X. Mao, Size-dependent brittle-to-ductile transition in silica glass nanofibers. *Nano Lett.* **16**, 105–113 (2016).
17. K. Zheng, C. Wang, Y. Q. Cheng, Y. Yue, X. Han, Z. Zhang, Z. Shan, S. X. Mao, M. Ye, Y. Yin, Electron-beam-assisted superplastic shaping of nanoscale amorphous silica. *Nat. Commun.* **1**, 1–8 (2010).
18. E. J. Frankberg, J. Kalikka, F. G. Ferré, L. Joly-Pottuz, T. Salminen, J. Hintikka, M. Hokka, S. Koneti, T. Douillard, B. Le Saint, Highly ductile amorphous oxide at room temperature and high strain rate. *Science* **366**, 864–869 (2019).
19. G. Wu, K. C. Chan, L. Zhu, L. Sun, J. Lu, Dual-phase nanostructuring as a route to high-strength magnesium alloys. *Nature* **545**, 80–83 (2017).
20. G. Wu, S. Balachandran, B. Gault, W. Xia, C. Liu, Z. Rao, Y. Wei, S. Liu, J. Lu, M. Herbig, W. Lu, G. Dehm, Z. Li, D. Raabe, Crystal-glass high-entropy nanocomposites with near theoretical compressive strength and large deformability. *Adv. Mater.* **32**, 2002619 (2020).
21. J. Zhang, Y. Liu, H. Yang, Y. Ren, L. Cui, D. Jiang, Z. Wu, Z. Ma, F. Guo, S. Bakhtiari, Achieving 5.9% elastic strain in kilograms of metallic glasses: Nanoscopic strain engineering goes macro. *Mater. Today* **37**, 18–26 (2020).
22. E. Ma, J. Ding, Tailoring structural inhomogeneities in metallic glasses to enable tensile ductility at room temperature. *Mater. Today* **19**, 568–579 (2016).
23. G. Wu, C. Liu, L. Sun, Q. Wang, B. Sun, B. Han, J. J. Kai, J. Luan, C. T. Liu, K. Cao, Y. Lu, L. Cheng, J. Lu, Hierarchical nanostructured aluminum alloy with ultrahigh strength and large plasticity. *Nat. Commun.* **10**, 1–8 (2019).
24. J. Wang, Q. Zhou, S. Shao, A. Misra, Strength and plasticity of nanolaminated materials. *Mater. Res. Lett.* **5**, 1–19 (2017).
25. D. Zhao, S. Wang, B. Zhu, L. Li, H. Zhao, Anisotropic deformation behaviors of amorphous-crystalline nanolaminates investigated via molecular dynamics simulations. *J. Alloys Compd.* **787**, 649–657 (2019).
26. M. C. Liu, J. C. Huang, Y. T. Fong, S. P. Ju, X. H. Du, H. J. Pei, T. G. Nieh, Assessing the interfacial strength of an amorphous-crystalline interface. *Acta Mater.* **61**, 3304–3313 (2013).
27. E. Alishahi, C. Deng, Orientation dependent plasticity of metallic amorphous-crystalline interface. *Comput. Mater. Sci.* **141**, 375–387 (2018).
28. M. W. Kapp, A. Hohenwarter, S. Wurster, B. Yang, R. Pippan, Anisotropic deformation characteristics of an ultrafine- and nanolamellar pearlitic steel. *Acta Mater.* **106**, 239–248 (2016).
29. C. R. Mayer, L. W. Yang, S. S. Singh, J. Llorca, J. M. Molina-Aldareguia, Y. L. Shen, N. Chawla, Anisotropy, size, and aspect ratio effects on micropillar compression of Al SiC nanolaminate composites. *Acta Mater.* **114**, 25–32 (2016).
30. J. R. Greer, J. T. M. De Hosson, Plasticity in small-sized metallic systems: Intrinsic versus extrinsic size effect. *Prog. Mater Sci.* **56**, 654–724 (2011).
31. W. Zhu, J. Liu, S. Mao, X. Wei, A new continuum model for viscoplasticity in metallic glasses based on thermodynamics and its application to creep tests. *J. Mech. Phys. Solids* **146**, 104216 (2021).
32. Y. Huang, *A User-Material Subroutine Incroporating Single Crystal Plasticity in the ABAQUS Finite Element Program* (Harvard Univ., 1991).
33. F. Delannay, The role of grain boundary mobility in diffusional deformation. *J. Mech. Phys. Solids* 104512 (2021).
34. Z. Liu, R. Li, G. Liu, W. Su, H. Wang, Y. Li, M. Shi, X. Luo, G. Wu, T. Zhang, Microstructural tailoring and improvement of mechanical properties in CuZr-based bulk metallic glass composites. *Acta Mater.* **60**, 3128–3139 (2012).
35. Y. Wu, Y. Xiao, G. Chen, C. T. Liu, Z. Lu, Bulk metallic glass composites with transformation-mediated work-hardening and ductility. *Adv. Mater.* **22**, 2770–2773 (2010).
36. W. Song, Y. Wu, H. Wang, X. Liu, H. Chen, Z. Guo, Z. Lu, Microstructural control via copious nucleation manipulated by in situ formed nucleants: Large-sized and ductile metallic glass composites. *Adv. Mater.* **28**, 8156–8161 (2016).
37. S. S. Jiang, Y. J. Huang, F. F. Wu, P. Xue, J. F. Sun, A CuZr-based bulk metallic glass composite with excellent mechanical properties by optimizing microstructure. *J. Non Cryst. Solids* **483**, 94–98 (2018).
38. F. F. Wu, K. C. Chan, S. H. Chen, S. S. Jiang, G. Wang, ZrCu-based bulk metallic glass composites with large strain-hardening capability. *Mater. Sci. Eng. A* **636**, 502–506 (2015).

39. F. F. Wu, K. C. Chan, S. S. Jiang, S. H. Chen, G. Wang, Bulk metallic glass composite with good tensile ductility, high strength and large elastic strain limit. *Sci. Rep.* **4**, 5302 (2014).
40. D. C. Hofmann, J. Y. Suh, A. Wiest, G. Duan, M. L. Lind, M. D. Demetriou, W. L. Johnson, Designing metallic glass matrix composites with high toughness and tensile ductility. *Nature* **451**, 1085–1089 (2008).
41. G. Chen, J. L. Cheng, C. T. Liu, Large-sized Zr-based bulk-metallic-glass composite with enhanced tensile properties. *Intermetallics* **28**, 25–33 (2012).
42. F. Szuecs, C. Kim, W. Johnson, Mechanical properties of $Zr_{56.2}Ti_{13.8}Nb_{5.0}Cu_{6.9}Ni_{5.6}Be_{12.5}$ ductile phase reinforced bulk metallic glass composite. *Acta Mater.* **49**, 1507–1513 (2001).
43. H. Zhai, H. Wang, F. Liu, A strategy for designing bulk metallic glass composites with excellent work-hardening and large tensile ductility. *J. Alloys Compd.* **685**, 322–330 (2016).
44. L. Zhang, Y. Wu, S. Feng, W. Li, H. Zhang, H. Fu, H. Li, Z. Zhu, H. Zhang, Rejuvenated metallic glass strips produced via twin-roll casting. *J. Mater. Sci. & Technol.* **38**, 73–79 (2020).
45. Z. W. Zhu, S. J. Zheng, H. F. Zhang, B. Z. Ding, Z. Q. Hu, P. K. Liaw, Y. D. Wang, Y. Ren, Plasticity of bulk metallic glasses improved by controlling the solidification condition. *J. Mater. Res.* **23**, 941–948 (2008).
46. J. R. Rice, Inelastic constitutive relations for solids: An internal-variable theory and its application to metal plasticity. *J. Mech. Phys. Solids* **19**, 433–455 (1971).
47. J. W. Hutchinson, Bounds and self-consistent estimates for creep of polycrystalline materials. *Proc. R. Soc. Lond.* **348**, 101–127 (1976).
48. Y. J. Wang, J. P. Du, S. Shinzato, L. H. Dai, S. Ogata, A free energy landscape perspective on the nature of collective diffusion in amorphous solids. *Acta Mater.* **157**, 165–173 (2018).

Acknowledgments

Funding: S.Z. acknowledges the financial support from the National Natural Science Foundation of China (nos. 51771201 and 52071124), the key project of the Natural Science Foundation of Tianjin (no. 20JCZDJC00440), and the key project of Natural Science Foundation of Hebei (No. E2021202135). K.M. acknowledges the financial support from the National Natural Science Foundation of China (no. 52002109), the National Natural Science Foundation of the Hebei province (no. E2020202088), and the Overseas Scientists Sponsorship Program by Hebei Province (C20210331). X.W. thanks the support from the National Natural Science Foundation of China (nos. 11772003, 11890681, and 11988102). Z.Z. acknowledges the financial support from the National Natural Science Foundation of China (no. 52074257). This research was also financially supported by the Open Research Fund from the State Key Laboratory of Rolling and Automation, Northeastern University, grant no. 2020RALKFKT002. B.W. and J.W. appreciate the support from the US National Science Foundation (CMMI- 2132336/2132383). P.K.L. very much appreciates the support from the US National Science Foundation (DMR-1611180 and 1809640). **Author contributions:** J.W., S.Z., and K.M. designed the research and wrote the first draft of this manuscript. Z.Z. prepared all samples and performed EBSD characterizations. K.M. and B.W. performed in situ SEM micropillars compression/tension tests and TEM observations. X.W., W.Z., and B.F. carried out theoretical analysis and numerical simulations. All the authors analyzed and interpreted the data and commented on the manuscript. **Competing interests:** The authors declare that they have no competing interests. **Data and materials availability:** All data needed to evaluate the conclusions in the paper are present in the paper and/or the Supplementary Materials.

Submitted 7 September 2021
Accepted 18 January 2022
Published 9 March 2022
10.1126/sciadv.abm2884